Bioresorbable Silicon Electronics for Transient Spatio-temporal Mapping of Electrical Activity from the Cerebral Cortex

Ki Jun Yu[1,2†], Duygu Kuzum[3,4,5†], Suk-Won Hwang[6], Bong Hoon Kim[2,7], Halvor Juul[8], Nam Heon Kim[2,7], Sang Min Won[1,2], Ken Chiang[9], Michael Trumpis[9], Andrew G. Richardson[4,10], Huanyu Cheng[11], Hui Fang[2,7], Marissa Thomson[3,4,12], Hank Bink[3,4], Delia Talos[8], Kyung Jin Seo[2,7], Hee Nam Lee[2,13], Seung-Kyun Kang[2,7], Jae-Hwan Kim[2,7], Jung Yup Lee[2,13], Younggang Huang[14], Frances E. Jensen[4,8], Marc A. Dichter[4,8], Timothy H. Lucas[4,10], Jonathan Viventi[9], Brian Litt [3,4,8*], John A. Rogers[1,2,7,*]

[1] *Department of Electrical and Computer Engineering, University of Illinois at Urbana-Champaign, Urbana, IL 61801, USA*

[2] *Frederick Seitz Materials Research Laboratory, University of Illinois at Urbana-Champaign, Urbana, IL 61801, USA*

[3] *Department of Bioengineering, University of Pennsylvania, Philadelphia, Pennsylvania 19104, USA*

[4] *Center for Neuroengineering and Therapeutics, University of Pennsylvania, Philadelphia, PA 19104, USA*

[5] *Department of Electrical and Computer Engineering, University of California, San Diego, San Diego, CA 92093*

[6] *KU-KIST Graduate School of Converging Science and Technology, Korea University, Seoul 136-701, Republic of Korea*

[7] *Department of Materials Science and Engineering, University of Illinois at Urbana-Champaign, Urbana, IL 61801, USA*

[8] *Department of Neurology, Perelman School of Medicine, University of Pennsylvania, Philadelphia, PA 19104, USA*

[9] *Department of Biomedical Engineering, Duke University, Durham, NC 27708, USA*

[10] *Department of Neurosurgery, Perelman School of Medicine, University of Pennsylvania, Philadelphia, PA 19104, USA.*

[11] *Department of Engineering Science and Mechanics, Penn State University, University Park, PA 16802, USA.*

[12] *Department of Chemical and Biomolecular Engineering University of Pennsylvania, Philadelphia, Pennsylvania 19104, USA*

[13] *Department of Chemical and Biomolecular Engineering, University of Illinois at Urbana-Champaign, Urbana, IL 61801, USA*

[14] *Department of Mechanical Engineering and Department of Civil and Environmental Engineering, Northwestern University, Evanston, IL 60208, USA*

[†]*These authors are contributed equally to this work.*
**To whom correspondence should be addressed. E-mail: jrogers@illinois.edu or littb@upenn.edu*

Supplementary Note 1: *In vitro* experiments of phosphorus doped Si NM electrodes

Results of impedance measured on devices constructed using Si NMs with different dopant species and concentrations (phosphorus, between ~10^{17} and ~10^{20}/cm^3; and boron, at ~10^{20}/cm^3) are comparable at all frequencies, up to ~1 kHz. (Supplementary Figs 4 and 5). The impedances measured from Si NMs with different thicknesses across a relevant range also show similar values (Supplementary Fig. 6), thereby suggesting an ability for continuous, reliable neural recording even as the electrodes dissolve over time. The doping level and the thickness do, however, strongly affect the time for complete dissolution, where increasing the level and thickness increases the lifetime. The impedance decreases, as expected, inversely with the areas of the electrodes (phosphorous, ~10^{20}/cm^3), as illustrated in the data of Supplementary Fig. 7 for dimensions of 200×200 μm^2 (A1), 300×300 μm^2 (A2), 400×400 μm^2 (A3), 500×500 μm^2 (A4).

Supplementary Note 2: Operation of the multiplexing on a representative unit cell

Supplementary Figs 16-18 summarize the key aspects of the designs of circuits that incorporate these transistors for multiplexed addressing. The approach involves two transistors per unit cell[12,14], in which a buffer transistor connects to the interface electrode to provide buffering of measured biopotentials, and a multiplexing transistor allows electrodes in a given column to share a single output wire. The surface electrodes appear in the top layer, where they come into physical contact with the brain; they connect to the underlying backplane circuit through vertical interconnect access holes (vias). An active shielding scheme described in Supplementary Fig. 18 improves the signal to noise ratio of the system by reducing the parasitic capacitance and increases the gain of each site of the electrodes. The operation involved successive application of 3V (V_r) to

the gate of the multiplexing transistor when a particular row was activated and -3V (V_r) when the row was not selected (Supplementary Figs 16 and 17). A constant current of 4 μA was used to bias the column output and complete the source follower amplifier. The output voltage (V_c) was high-pass filtered to have an average DC bias of 2V and connected to the column power source line (V_{as}). By using analog feedback, the negative effects of parasitic capacitance in the drain of the buffer transistor are reduced and the AC signal gain of the electrode array is improved. A 50 Hz, 200 mV (peak to peak) sinusoidal waveform was applied to a metal reference electrode immersed in PBS at pH 7.4 and recorded from the active electrode array (Supplementary Fig. 19). During multiplexed sampling, driving the row select signal selects a single row of electrodes at a time. This scheme allows the unit cells in the corresponding row to drive the column output lines which connect to a high-speed analog to digital converter. Row select signals are rapidly cycled to sample all electrodes on the array. The entire device connects to an external data acquisition (DAQ) system through a zero insertion force (ZIF) connector with 26 contact.

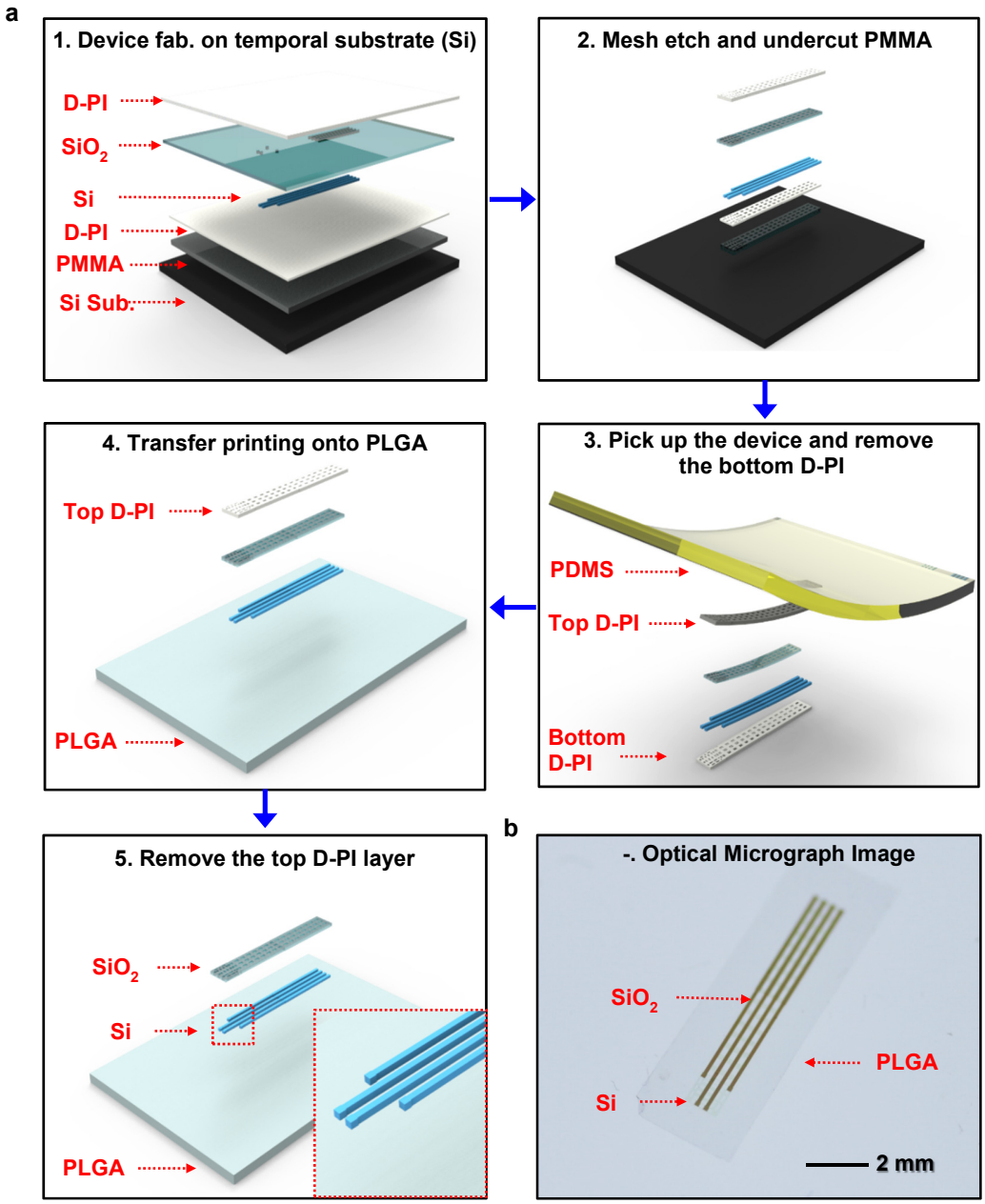

Supplementary Figure S1 | Materials and procedures for fabricating bioresorbable passive electrodes on biodegradable substrates (PLGA) and a device image. (a) Schematic illustrations of key processes for fabricating bioresorbable passive electrodes: (1) printing highly n-doped Si on temporary substrates, (2) defining the mesh structure, followed etching by RIE and immersion buffered oxide etchant (BOE), (3) retrieving the device onto a PDMS slab, (4) printing the device onto a bioresorbable substrate (PLGA), and (5) removing the top D-PI layer. (b) Optical image of a complete device.

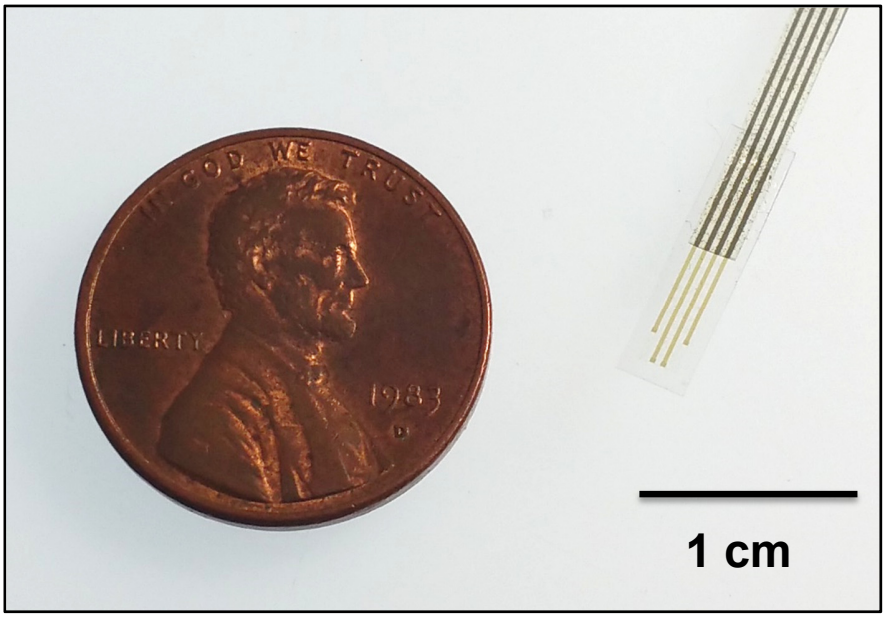

Supplementary Figure S2 | A photograph of a bioresorbable passive electrode array with a penny.

a

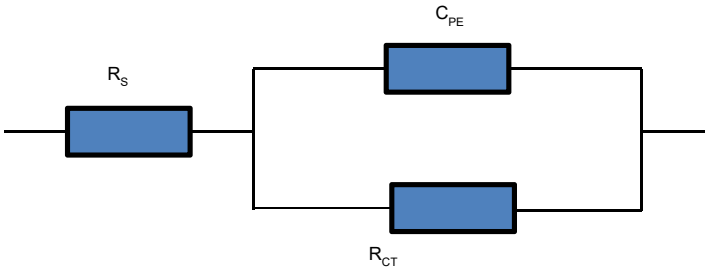

b

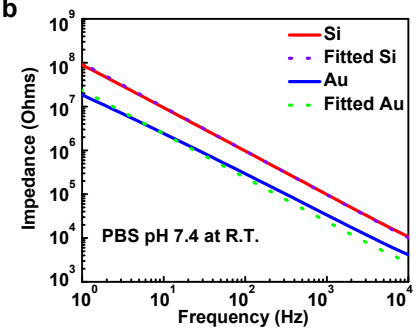

c

	C_{PE}	R_{CT}
Si	2.5 μF/cm^2	4 G-ohms
Au	10 μF/cm^2	0.3 G-ohms

Supplementary Figure S3 | EIS characterization of Si and Au. (a) Schematic description of the equivalent circuit model used to fit EIS measurement results. C_{PE} is the constant phase element representing the double-layer capacitance; R_{CT} is the charge transfer resistance; and R_S is the solution resistance. (b) Results of measurement (solid lines) and fitting (dashed lines) for the impedance. (c) Representative values of C_{PE} and R_{CT} for Au and Si.

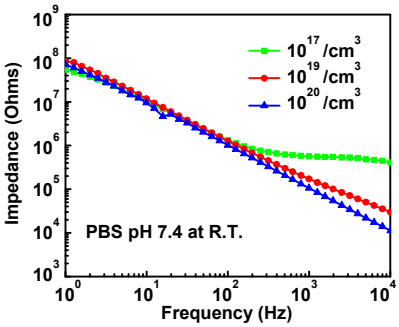

Supplementary Figure S4 | Impedance spectra of phosphorus doped Si NM electrodes with different doping concentrations (10^{17} /cm^3, 10^{19} /cm^3, 10^{20} /cm^3).

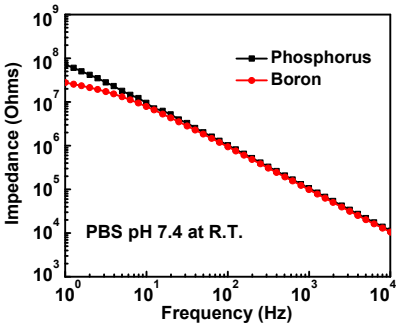

Supplementary Figure S5 | Impedance spectra of boron and phosphorus doped Si NM electrodes with the same doping concentrations (10^{20} /cm^3) for both boron and phosphorus.

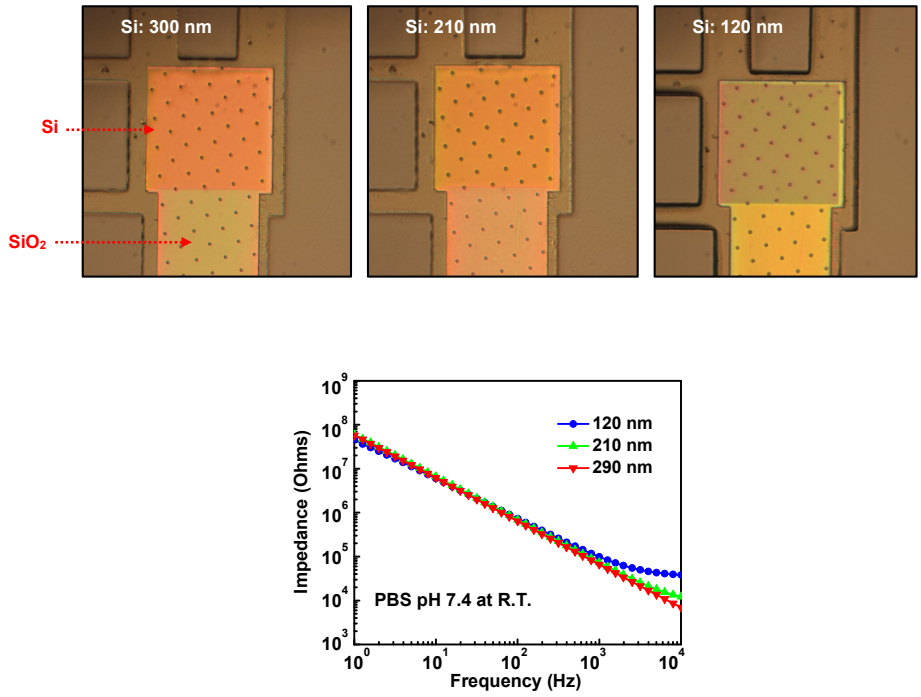

Supplementary Figure S6 | Impedance spectra of different thicknesses (300 nm, 210 nm, 120 nm) of sites of Si.

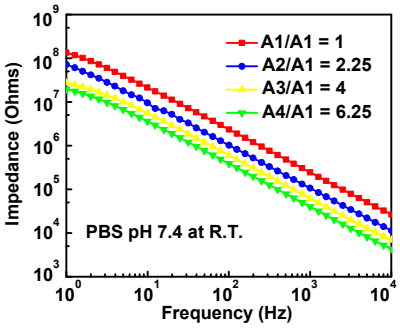

Supplementary Figure S7 | Impedance spectra of phosphorus doped Si NM electrodes with the different areas (200×200 μm^2 (A1), 300×300 μm^2 (A2), 400×400 μm^2 (A3), 500×500 μm^2 (A4)) of sites.

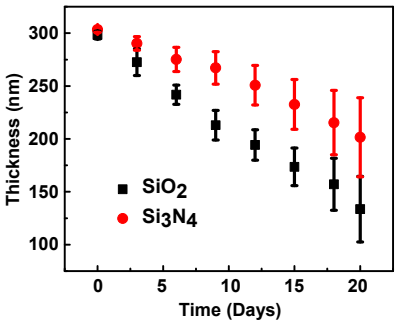

Supplementary Figure S8 | Hydrolysis kinetics for SiO_2 and Si_3N_4 used in the devices. Thicknesses as a function of time during dissolution in artificial cerebrospinal fluid (ACSF) at 37 °C. The initial thicknesses were 300 nm for both SiO_2 and Si_3N_4.

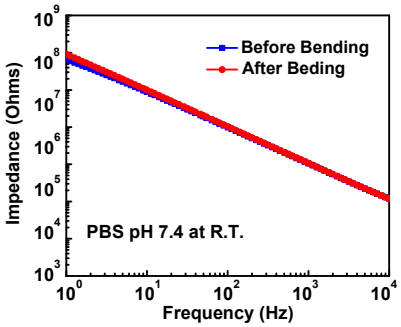

Supplementary Figure S9 | Impedance spectra of before and after bending with 2 mm bending radius of a bioresorbable passive electrode array.

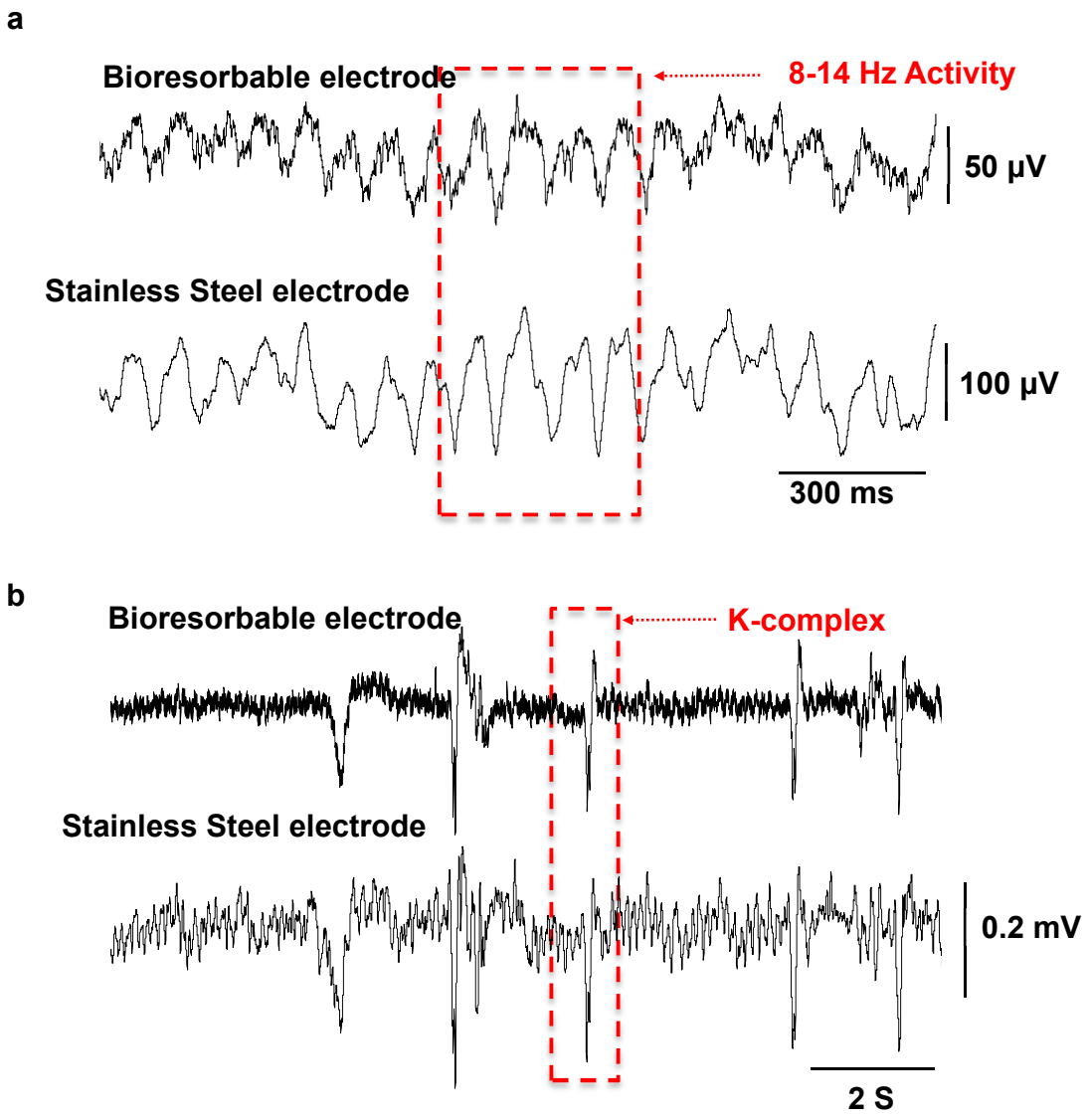

Supplementary Figure S10 | *In vivo* neural recordings in rats. (a) Slow wave activity and (b) k-complexes recorded using a bioresorbable electrode array and a control stainless steel microwire electrode.

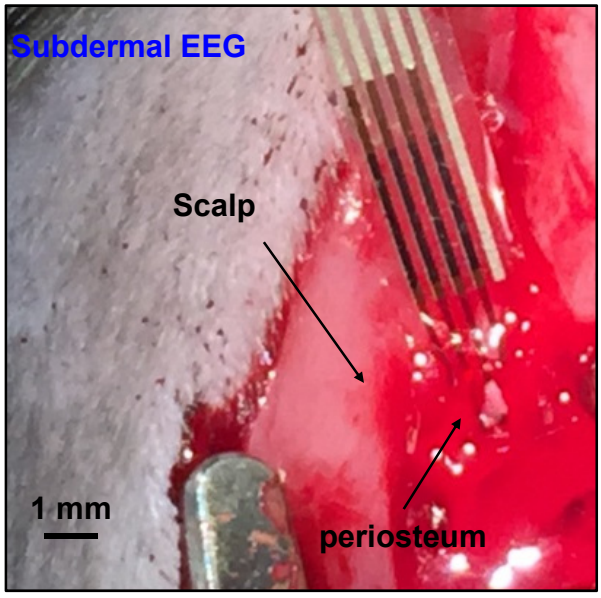

Supplementary Figure S11 | A photograph of bioresorbable passive electrode array placed onto the periosteum of a rat.

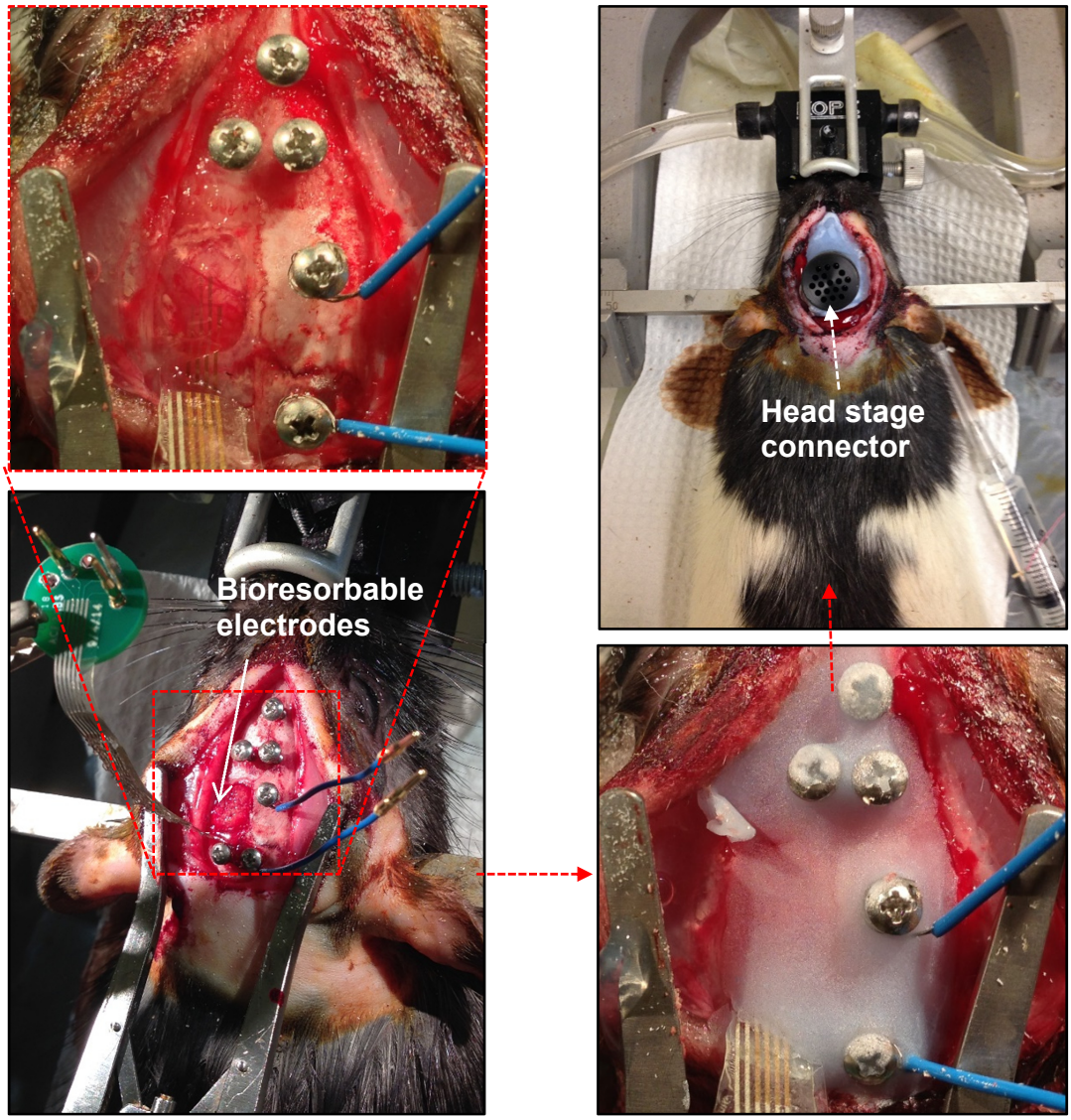

Supplementary Figure S12 | Photographs of surgery associated with chronic recording experiments. Implanting the bioresorbable electrode arrays on a rat brain, applying the dental cement, and then burying the head stage board.

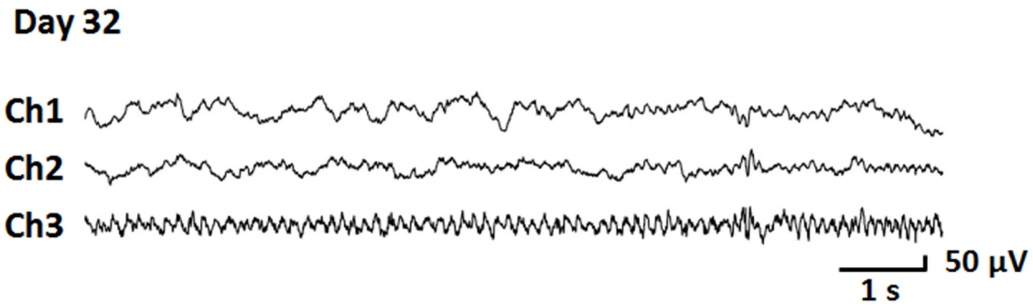

Supplementary Figure S13 | Representative ECoG signals recorded by the bioresorbable array (Ch1, Ch2, and Ch3) and the control electrode on day 32.

Supplementary Figure S14 | A photograph after the surgery of the device implantation, showing freely moving rat with a head stage connector.

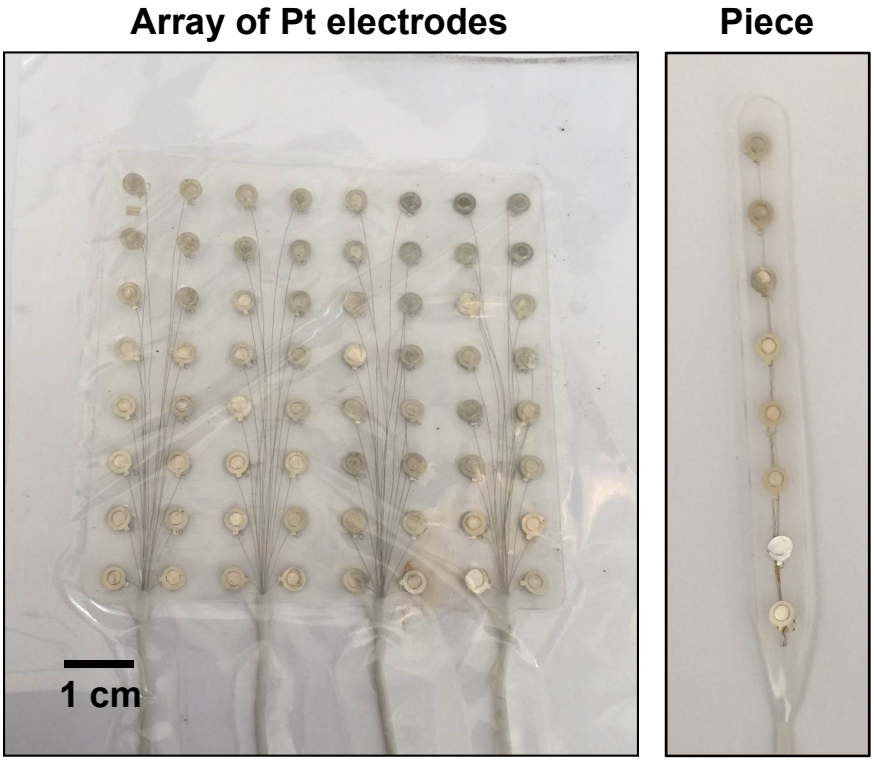

Supplementary Figure S15 | Clinical platinum electrodes for ECoG, 8 × 8 Electrode Grid (left), and 1 × 8 Strip Electrode (right).

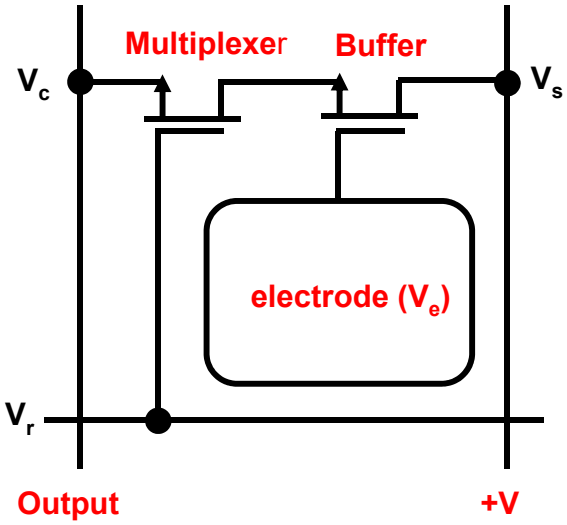

Supplementary Figure S16 | Schematic circuit diagram of a single unit cell containing two matched n-MOS transistors in an actively multiplexed, bioresorbable electrode array.

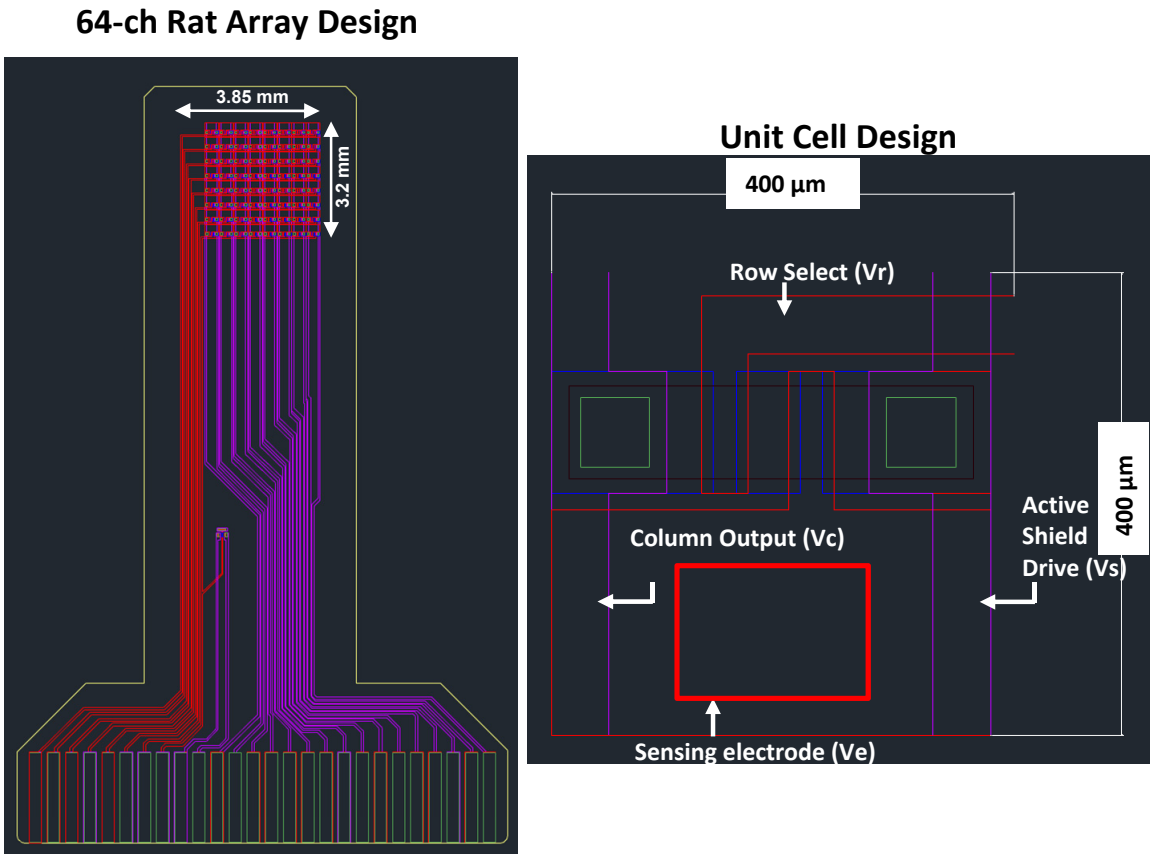

Supplementary Figure S17 | Schematic illustration of a 8×8 array of actively multiplexed channels, showing the entire device (left), and the unit cell design (right).

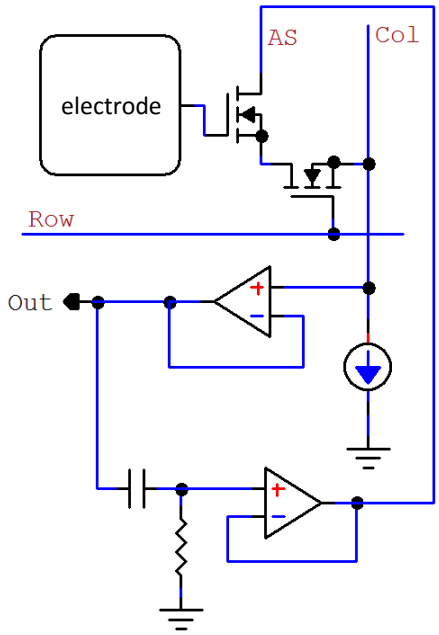

Supplementary Figure S18 | Schematic circuit diagram for an active shielding circuit for the actively multiplexed array.

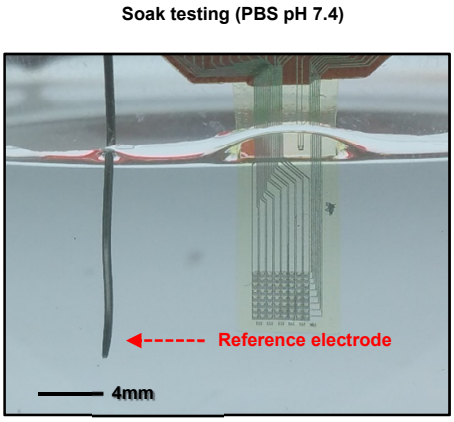

Supplementary Figure S19 | *In vitro* test setup for actively multiplexed array.

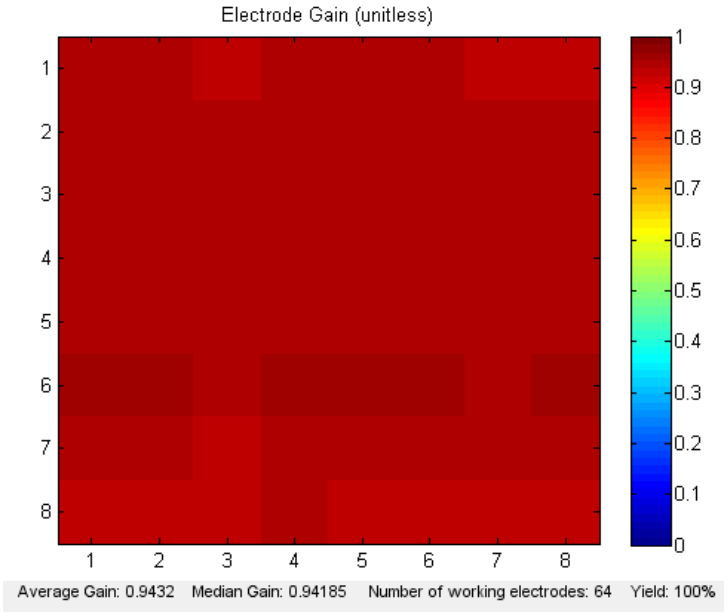

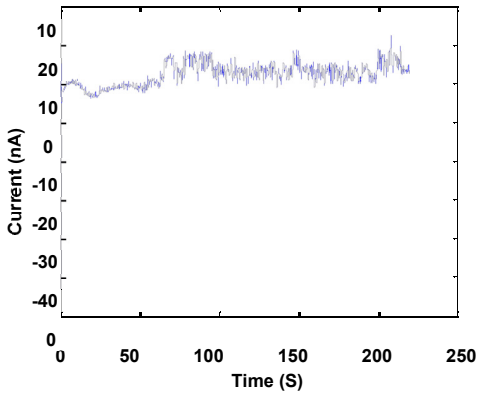

Supplementary Figure S20 | Color map illustrating the spatial distribution of the electrode response, demonstrating the spatial uniformity of the gain of an actively multiplexed, bioresorbable electrode array and leakage current over time.

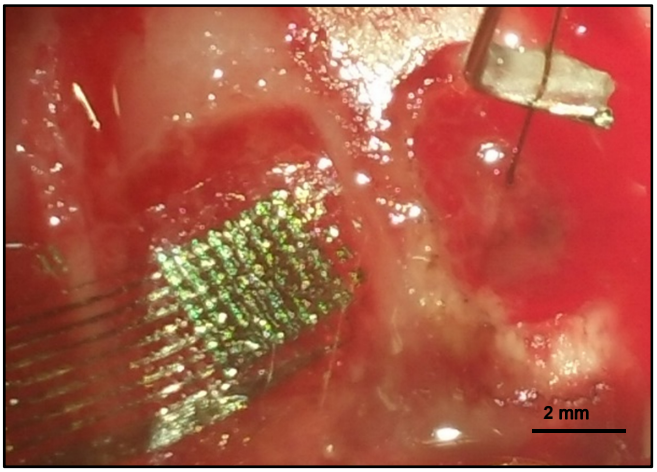

Supplementary Figure S21 | Photograph of an implanted 8x8 actively multiplexed array (left hemisphere of rat brain) and a control electrode (right hemisphere of rat brain).

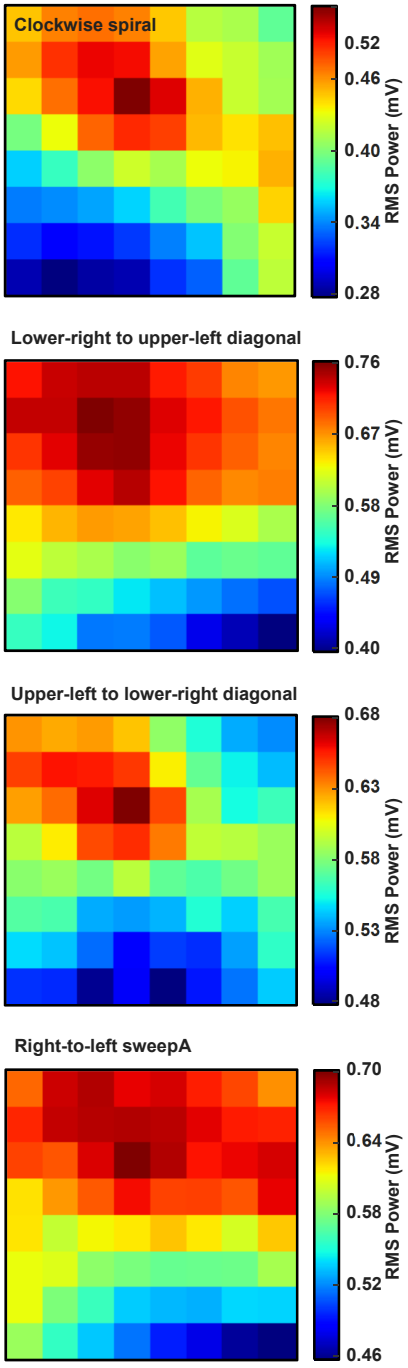

Supplementary Figure S22 | Representative RMS power image maps from four different spike clusters (clockwise spiral, lower-right to upper-left diagonal, upper-left to lower-right diagonal, right-to-left sweep) illustrate the high sensitivity of the electrode array and the spatially localized nature of spikes.

Nutrients	Mo	P	SiO_2
Recommended Daily Intakes	45 mcg	700 mg	5-10mg
Upper Limits	2000mcg	4g	N/A

Element	Si (Source: food)
Average Daily Intakes	20-50 mg

Compound	Ammonia (byproduct of Si_3N_4)
Amount of Daily Production	17 g
In the blood	0.7-2 mg/L

*The amount of Si_3N_4 in a device is 264 mcg. The amount of ammonia generated by dissolution of the Si_3N_4 is 128.2 mcg.
*Literature studies report a geographical correlation between the prevalence of Alzheimer's disease (AD) or various adverse effects on the central nervous system (CNS) in human brain and the concentration of aluminium ions (Al) in the brain from drinking water supplies[5,6]. The level of Al ions in the body can be significantly reduced by $SiOH_4$ (byproduct of dissolution of Si and SiO_2) by forming hydroxy-aluminosilicates (HAS)[6]. Studies also suggest that silicon-rich mineral waters can reduce the burden of aluminium in both Alzheimer's patients and control group[7].

Supplementary Table 1 | Recommended daily intake and upper limits[1] for injestion of Mo, P and SiO_2, average daily intake of Si from food[2,3], and amounts in the blood and daily production of ammonia for adults[4].

References

1. http://iom.nationalacademies.org/Activities/Nutrition/SummaryDRIs/DRI-Tables.aspx

2. Pennington, J. A. T. Silicon in foods and diets Food. *Addit. Contam.* **8**, 97-118 (1991).

3. Jugdaohsingh, R. *et al*. Dietary silicon intake and absorption. *Am. J. Clin. Nutr.* **75**, 887–893 (2002).

4. Syracus research coporations. Toxicological profile for ammonia. (2004).

5. Kawahara, M, & Kato-Negishi, M. Link between aluminum and the pathogenesis of Alzheimer's Disease: the integration of the aluminum and amyloid cascade hypotheses. *Int. J. Alzheimer's Dis.* **2011**,276393 (2011).

6. Jurkic, L. M., Cepanec, I., Pavelic, S. K., & Pavelic, K. Biological and therapeutic effects of ortho-silicic acid and some ortho-silicic acid-releasing compounds: new perspectives for therapy. *Nutr. Metab*. **10**, 2-12 (2013).

7. Davenward, S. *et al*. Silicon–rich mineral water as a non-invasive test of the 'aluminum hypothesis' in Alzheimer's disease. *J Alzheimers Dis*. **33**, 423–430 (2013).